Model of Reflectance of Thermophotovoltaic Cell and Cold Plate

by

Lucy Milde

Submitted to the
Department of Mechanical Engineering
in Partial Fulfillment of the Requirements for the Degree of

Bachelor of Science in Mechanical Engineering

at the

Massachusetts Institute of Technology

May, 2020

Signature of Author: _____

Department of Mechanical Engineering
May 14, 2020

Certified by: _____

Asegun Henry
Associate Professor of Mechanical Engineering
Thesis Supervisor

Accepted by: _____

Maria Yang
Professor of Mechanical Engineering
Undergraduate Officer

Model of Reflectance of Thermophotovoltaic Cell and Cold Plate

by

Lucy Milde

Submitted to the Department of Mechanical Engineering
on May 14, 2020 in Partial Fulfillment of the
Requirements for the Degree of

Bachelor of Science in Mechanical Engineering

ABSTRACT

The reflectivity of a gold-plated cold plate, and mounted multi-junction photovoltaic cells, is studied in the context of a thermal energy grid storage system. The emitter is modeled as a black body emitter. Improving the efficiency of the system requires high reflectance below the bandgap energy of the cells, and high absorption above the bandgap. The matrix transfer method is used to predict the total reflectance of the cell, and to study the effect of changing the thickness of the most significant layer. Decreasing the thickness of this layer can lead to a higher reflectance below the bandgap, but more data is needed to fully integrate the effect of doping concentration (using the Drude model) into these reflectance calculations.

Thesis Supervisor: Dr. Asegun Henry
Title: Associate Professor of Mechanical Engineering

Acknowledgements

Thank you to Professor Henry, Alina LaPotin, and Colin Kelsall for their guidance on this thesis, and support throughout an unusual semester.

Table of Contents

List of Figures

List of Tables

1. Introduction

1.1 Motivation

Large increases in solar and wind are straining wholesale energy markets, due to low or nonexistent variable operating costs and intermittent production. The daily timings of renewable energy sources do not align with industrial and domestic peak use of electricity, leading to very low prices during the middle of the day, and extremely high prices in the evenings. Wholesale electricity prices ranging from unusually high to negative is economically challenging to traditional base load generators, and instead favors flexible gas turbines [1]. While these turbines allow the grid to meet peak demand, they are incompatible with a carbon free grid (baring potential carbon capture.) Turbine based plants incur significant fatigue damage each time they lower and raise output due to cyclic thermal loading, and so are incentivized to remain on line even when market prices are below their variable operating cost [2]. These peaker plants must be replaced with dispatchable carbon-neutral energy sources, such as stored wind or solar to fully decarbonize the grid. Pumped hydropower can fill part of this role, but its expansion is severely limited by geography. Although prices are lowering, batteries remain far too expensive to serve as grid scale energy storage systems. The ultra-high temperature thermal energy grid storage, using multi-junction photovoltaic (MPV) cells, discussed here has the potential to cost significantly less. The system, shown in Figure 1, uses electricity to heat liquid silicon from around 1900°C to 2400°C. After being stored in a large insulated tank, the silicon is pumped through graphite pipes (covered in tungsten foil.) These pipes emit photons, that are then converted to electricity in multi-junction photovoltaic cells, during times of high demand for electricity. The cells can be moved into, or out of, this incident radiation to control the system output. The cells cannot function at the same temperature as the tungsten emitter, and so are mounted onto an actively cooled block, referred to here as the cold plate [3]. This system could allow for a much higher rate of renewable penetration of electrical grids, but requires high efficiency conversions from thermal to electrical energy.

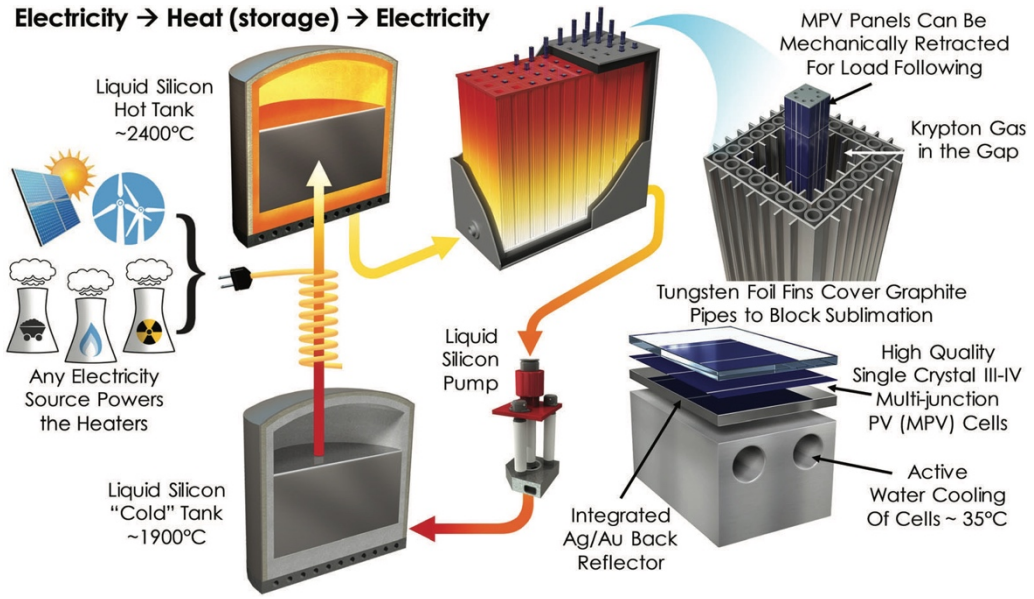

Figure 1 Schematic showing thermal energy grid storage with multi-junction photovoltaic cells. Amy, Caleb; Seyf, Hamid Reza; Steiner, Myles A.; Friedman, Daniel J.; and Henry, Asegun; *Thermal energy grid storage using multi-junction photovoltaics* Energy Environ. Sci., 2019, 12, 334, DOI: 10.1039/c8ee02341g, p 337.

1.2 Requirements of cold plate

Radiation is the primary mode of heat transfer between the hot fluid and the MPV cells. The cells will be mounted to a copper cold plate, with chilled water at 20° C continuously pumped through cooling channels under each cell. The cold plate will also have many channels to support a sweeping noble gas curtain over the cells to prevent deposition of tungsten onto the cells. The cold plate must maintain at an optimum operating temperature for the cells, and prevent extreme overheating that could cause welded joints to fail and allow pressurized water to escape. While cells will be mounted on four sides of the cold plate, some inactive surface area will remain exposed to radiation. Ideally, all radiation incident onto inactive surfaces will be reflected, preventing unused thermal energy from moving through the cold plate into the coolant and exiting the system. Radiation below the band gap energy landing on cells should also be reflected, and this will be affected by the composition of layers in the cell, as well as the gold cell backing. Measuring this reflectance and parasitic heat loss in the cold plate is necessary to predict the efficiency of the system.

2. Measurement of Heat Flux

This ideal reflectance profile would lead to an efficient cell, and minimize the active cooling needed to maintain the operating temperature of the cells. This will be measured on an experimental cold plate and MPV cell system that is smaller than a full scale commercial version of the system, and has a much lower ratio of active area to total area exposed to radiation. This makes representative measurements of the parasitic heat loss in active areas challenging, but crucial, to measure. Two methods for experimentally determining this heat flux were considered: heat flux sensors and a cold plate colorimeter.

2.1 Heat Flux Sensors

The heat flux sensor will be placed between the cell and the cold plate, allowing for the measurement of thermal energy parasitically absorbed through the cell, and will not be affected by the low ratio of active to inactive area on the small setup. This is the primary appeal of using a sensor, but it is accompanied by its own challenges. Although the sensors themselves have extremely low thermal resistance, a thermal interface material is needed to support adequate thermal conduction between the sensor and the cell, as well as the sensor and the cold plate. These materials are in series, and thermal resistances are added. This will inevitably keep the cells at a higher temperature than without sensing, but an additional ΔT of 20° C is acceptable. Using the following relation, with approximate heat flux, $\dot{Q}$, as $10^6 \frac{W}{m^2}$, it is determined that each thermal interface material must have a resistance, R_{TIM}, below $10^{-5} \frac{m^2 K}{W}$.

$$2 R_{TIM} \dot{Q} = \Delta T \quad (1)$$

A number of pastes are commercially available, and with listed thermal conductivity values. From this property, and the requirement for thermal resistance, a maximum thickness can be calculated. For the seven pastes considered, this ranged from 0.007 to 0.7 mm. A thermal pad, with thickness 0.5 mm, and resistance $8.3 \times 10^{-5} \frac{m^2 K}{W}$, was also considered [4]. The thermal

resistance is proportional to thickness, so the thickness of the paste must be carefully measured to prevent the cell from unexpectedly reaching a component's melting temperature.

Commercially available heat flux sensors are available, but the extreme heat flux and small size of this application severely limit the options. The companies Omega and GreenTEG both offer products with low sensitivity, but are limited in range to $\pm 150 \frac{\mathrm{kW}}{\mathrm{m}^2}$, an order of magnitude below the expected heat flux. FluxTeq product HTHFS-01 is able measure this heat flux, if kept below 1000°C. The sensing area of this model is 0.39 by 0.22 inches, much smaller than the one square centimeter cell [5]. The sensor is 0.125 inches thick, requiring the space around the sensor to be filled with thermal interface material to maintain thermal equilibrium between the entire cell and the cold plate. A similar sizing issue is present with products from the International Thermal Instrument Company [6]. Additionally, wires must be properly insulated from the sensors to outside of the hot zone where the data can be collected.

2.2 Calorimeter

A calorimeter measures the heat loss by comparing the temperature of the cooling water as it enters and exits the cold plate. After the system has reached steady state, this calculation will measure the total thermal energy absorbed by the entire cold plate and cells. Although the relative temperatures of the water at the inlet and outlet can be fairly accurately measured, it is challenging to determine if the losses are coming through the active cell area or the inactive area. Collecting data for two cases, with and without a cell, will reduce uncertainty on this. Assuming radiation is evenly distributed on the surface of the cold plate without TPV cells, the proportion of heat loss through the (always) inactive area will be equal to the proportion of surface area that will remain inactive once the TPV cells are added. This value for heat loss through inactive area can then be subtracted from the heat loss of the cold plate with TPV cells, leaving only the parasitic heat loss from the active area of the TPV cells. Although this calculation introduces additional uncertainty into the measurement of heat flux, it relies on a more robust experimental setup than using heat flux sensors, and so is chosen to pursue farther. The rest of this paper explores ways to minimize this parasitic heat loss being measured.

3. Reflectivity and Optical Depth of Gold

An essential tool to maintain a high efficiency of the system is gold plating on the surface of the cold plate, to increase the reflectance. Because gold is highly reflective over the emitter spectrum (0.4 μm to 20 μm), it will help keep the cell cool, while conserving the thermal energy of the system. Gold will cover all inactive area on the cold plate, as a high reflectance at relevant wavelengths is desired. The gold plating must be optically thick enough that the underlying copper does not affect the reflectance. Energy propagation decays exponentially in a media as it is absorbed, and decreases by e^{-1} at the skin depth (δ), which is the inverse of the absorption coefficient [7].

$$\delta = \frac{\lambda}{4\pi k} \tag{2}$$

In this equation, λ is the wavelength (of the radiation) and k is the extinction coefficient, which is a wavelength dependent optical property of the material. For gold, over relevant wavelengths, the skin depth ranges from approximately 22 to 47 nm [8]. Based on this value, and an expectation for variation in quality from the electroplating process, a set of samples were ordered from a local electroplater. One inch by one inch tiles were cut from copper with a mirror finish on one side, and an unfinished surface on the other. An asymmetric notch allowed the two sides to be clearly distinguished after plating. The samples were nominally plated with gold of thickness 25, 50, 100, 200, 300, 400, and 500 nm. A fourier-transform infrared spectroscopy (FTIR) machine will be used to measure the reflectance across wavelengths from 0.1 to 10 micrometers. It is expected that all samples with films greater than 100 nm will behave as an optically thick material, as this is more than twice the largest skin depth, but inaccurate gold thicknesses may cause variance in the reflectance. The surface finish of the copper affects the surface finish of the gold, so the mirror-finished sides of the samples may exhibit higher reflectance, than the unfinished sides, at all wavelengths. This data will inform selecting a thickness of gold for the final cold plate. For low quantity production, gold plating costs around $0.40 per 100nm thickness over one square centimeter [9]. The total cost increases linearly, and so minimizing the thickness is preferred.

4. Cell Reflectance Model

4.1 Spectral Radiance

The cavity emitter geometry provides the opportunity for photons with energy below the bandgap of the TPV cell to be recycled by using a high quality back surface reflector (BSR.) A cell that includes a BSR with reflectivity of one can have more than double the efficiency of a cell with no BSR [10]. Above bandgap radiation is either converted to electricity or to heat (dependent on the internal quantum efficiency of the cell.) Below bandgap radiation will either be reflected or absorbed as heat, but cannot produce useful electricity. However, reflected photons can be re-emitted so do not count as an efficiency penalty. Any absorbed heat will leave the system through the coolant water, and represents an inefficiency in the system. An ideal MPV cell should have high reflectance below the bandgap and low reflectance above the bandgap energy.

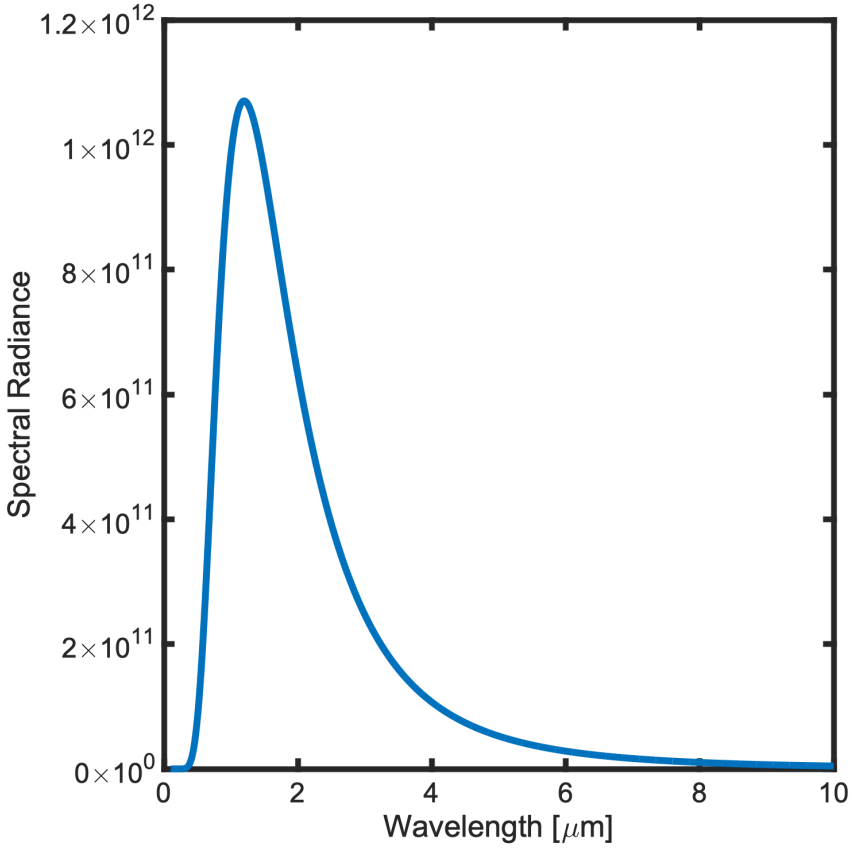

Figure 2 Spectral radiance of black body radiation at 2150°C.

The cell should be evaluated in the context of its operating environment. The cell will be exposed to a tungsten emitter (assuming an infinite area ratio between the emitter and the cell) modeled as a black body at 2150°C. The spectral radiance is dependent on universal constants, the temperature of the body, T, and can be evaluated at any wavelength. Figure 2 shows a measure of the intensity of light present, and it is important to consider the relative prominence of each wavelength when evaluating the reflectance of the cell under a range of wavelengths. The maximum value of spectral radiance is at 1.2 μm. Planck's constant, h, the speed of light in a vacuum, c, and Boltzmann constant, k_B, are also used to find spectral radiance, M_{sr}.

$$M_{sr} = \frac{2\pi hc^2}{\lambda^5}\left(e^{hc/\lambda T k_B} - 1\right)^{-1} \quad (3)$$

Table 1 Materials and thicknesses of layers in the multi-junction photovoltaic cell used in matrix calculations. Tabulated values for the dielectric constant as a function of wavelength were entered for each material. [11-14]

Thickness [m]	**Material**	**Layer No.**
semi infinite	Air	
0.15e-6	MgF_2	1
0.2e-6	GaInP	2
0.1e-6	AlGaInAs	3
3e-6	AlGaInAs	4
0.3e-6	GaInP	5
0.2e-6	AlGaInAs	6
0.125e-6	GaAsSb	7
0.1e-6	GaInAs	8
0.3e-6	GaInP	9
0.2e-6	GaInAs	10
2.5e-6	GaInAs	11
0.3e-6	GaInP	12
0.1e-6	GaInAs	13
semi infinite	gold	

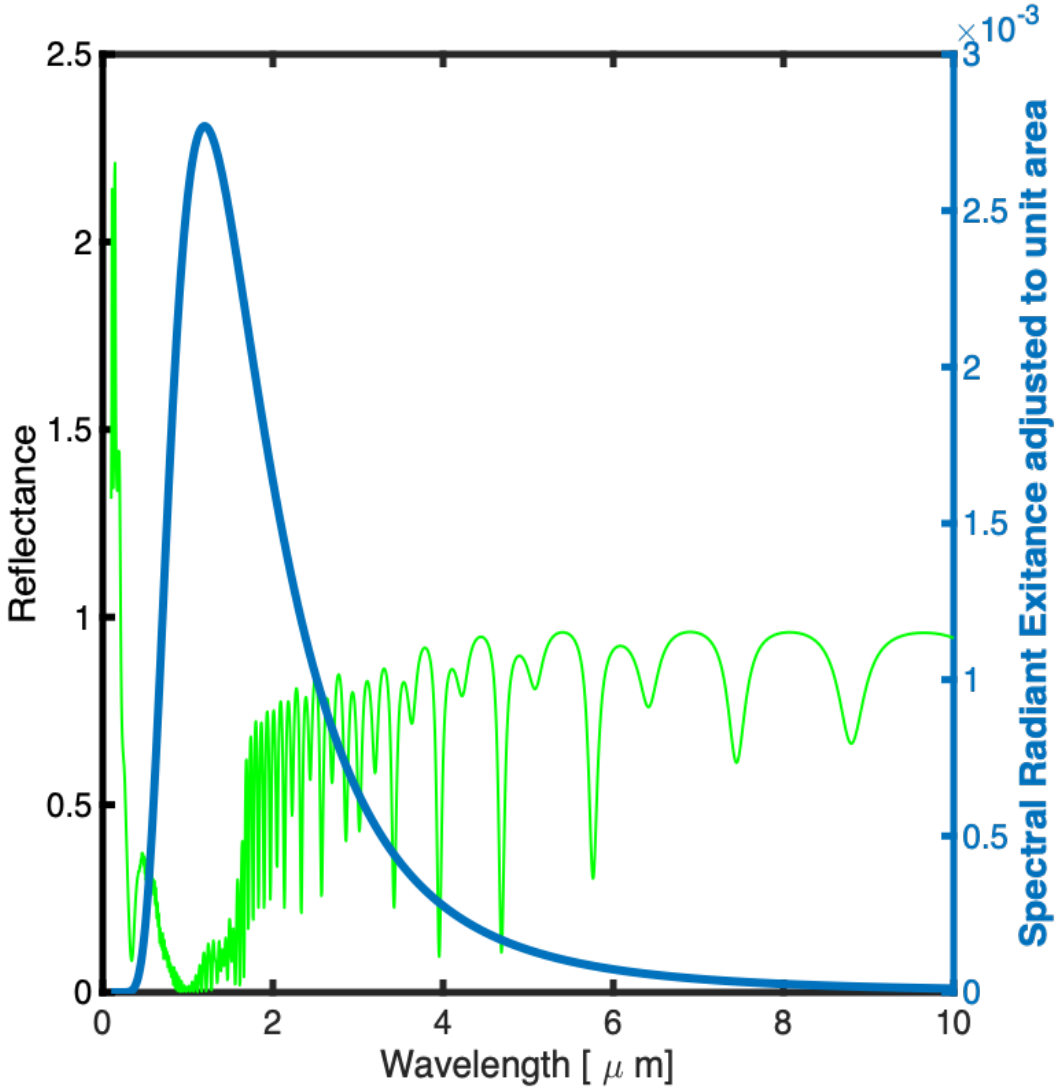

Figure 3 Reflectance and spectral radiance vs. wavelength [11-14].

4.2 Matrix Transfer Method for Cell Reflectance Calculations

The reflectance of the cell was calculated using the matrix transfer method for thin films. A transfer matrix is formed for each interface between layers in the cell, allowing for expansion to a fifteen layer cell. The wave vector normal to the interface surface can be calculated as

$$k_z = \sqrt{\varepsilon \left(\frac{\omega}{c}\right)^2 - \left(\frac{\omega}{c}\right)^2 \sin^2 \theta} \tag{4}$$

The complex dielectric constant is ε, while the frequency of the radiation, ω, and the speed of light, c, also contribute. With an angle of incidence (θ) of zero, this simplifies to a single term. The inputs to this model are layer thickness, d, and dielectric constant. The dielectric constant can be written in terms of refractive index, n, and extinction coefficient, k, as

$$\varepsilon = (n + ik)^2 \tag{5}$$

The amplitudes of the forward, A_j, and backwards, B_j, propagating waves in each layer, j, can be calculated with the values from the previous layer by writing expressions for the conservation of energy in each layer and at each interface [15].

$$A_j = e^{-ik_z d_j} A'_j \tag{6}$$

$$B_j = e^{ik_z d_j} B'_j \tag{7}$$

Using the transfer matrix method, the reflectance of the MPV cell (with materials and layer thickness listed in Table 1) was calculated. Figure 3 shows how the reflectance varies greatly across wavelengths. To find total reflectance, the reflectance, ρ, at each wavelength, λ, is integrated and weighted by the spectral radiance, M_{sr}. These calculations use $\lambda_1 = 0.1\ \mu$m and $\lambda_2 = 10\ \mu$m.

$$\rho_{total} = \frac{\int_{\lambda_1}^{\lambda_2} \rho(\lambda) M_{sr}(\lambda)\, d\lambda}{\int_{\lambda_1}^{\lambda_2} M_{sr}(\lambda)\, d\lambda} \tag{8}$$

4.3 Plasma Frequency

The plasma frequency should to be found to put the above calculations in context. Semiconductors act as metals when low frequency radiation is applied, reflecting nearly all energy. At the plasma frequency, ω_p, the semiconductor transitions to behaving more like an insulator, and the reflectance is much lower [16]. This application calls for reflecting wavelengths longer than the band gap wavelength, and transmitting as much radiation shorter than the bad gap wavelength as possible, so careful consideration of the plasma frequency is warranted. This transition occurs when the real component of the dielectric function equals zero, becoming positive at higher frequencies. (Some materials do not have a plasma frequency and the real component is always negative.) The doping concentration, of electrons or holes, is given by n. The relaxation time, τ, originates in the damping term of the equations of motion of the

electrons. The effective mass, m, is approximated as the mass of an electron, and e is the charge of an electron. The effects that are not included in the Drude model are accounted for in ε_{core} [16].

$$\varepsilon_1 = 0 = \varepsilon_{\text{core}} - \frac{4\pi \text{n} e^2 \tau^2}{m(1+\omega_p{}^2\tau^2)} \quad (9)$$

$$\omega_p{}^2 = \frac{4\pi n e^2}{m\varepsilon_{core}} - \frac{1}{\tau^2} \quad (10)$$

4.4 Limitations of current data

The above transfer matrix calculations have been made using tabulated values for the dielectric function as a function of wavelength. This accounts for the fact that semiconductors can behave very differently when exposed to high and low frequency radiation. However, these sources do not model changes in the dielectric function due to altering the electron or hole doping concentration of the materials.

The Drude model is a classical model that uses a few parameters to predict the effect of free carriers on the optical properties of the material. The model builds off of the drift velocity of the free carriers in an oscillating electric field, related by equations of motion [16]. The complex conductivity can be found using the current density and drift velocity. The relaxation time is again τ.

$$\sigma = \frac{ne^2\tau}{m(1-i\omega\tau)} \quad (11)$$

This method prioritizes studying the free carrier mechanism, which is dependent on complex conductivity from above [16]. The core dielectric constant, ε_{core}, is independent of doping concentration.

$$\varepsilon(\omega) = \varepsilon_{core} + \frac{4\pi i\sigma}{\omega} \quad (12)$$

The Drude model is dependent on electron doping concentration, as well as frequency, and so could add to the applications of this model [16]. Relaxation time is a material property, but is sparsely covered in the literature. Data on the dielectric constant requires additional information on the electron doping concentration of the material to be useful in fitting parameters to this

model. With experimental values of the complex electrical conductivity, σ_1, at frequency ω_1, and doping concentration n_1, τ for the material can be calculated as such.

$$\tau = \frac{\sigma_1}{n_1 e^2/m + i\sigma_1\omega_1} \tag{13}$$

With this value of relaxation time, a second reference point for the material is needed. The dielectric function, $\varepsilon_{complex2}$, at frequency ω_2, and known doping concentration n_2, can be used to solve for the core dielectric constant.

$$\varepsilon_{core} = \varepsilon_{complex2} - \frac{4\pi i\sigma_2}{\omega_2} \tag{14}$$

If data is available, the relaxation time and core dielectric constant should be calculated from multiple values of the conductivity and dielectric function, and then averaged. These constants complete the model and can be used to find the dielectric function depending on frequency and doping concentration [16].

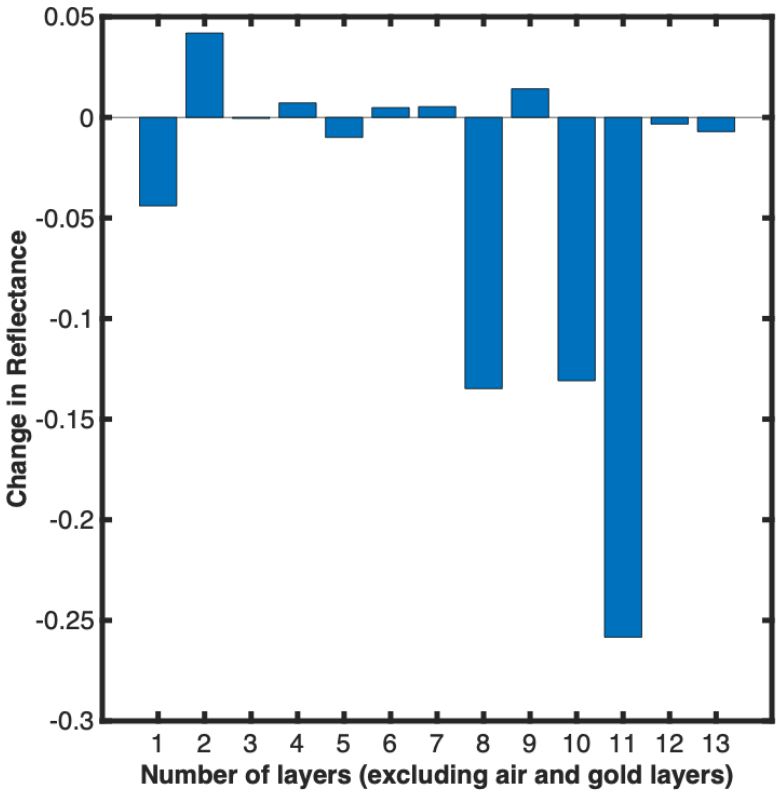

Figure 4 The relative change in reflectance from a cell (bounded by air and gold) when layer j is added to (j-1) existing layers.

$$\varepsilon = \varepsilon_{core} + \frac{4\pi i n e^2 \tau}{\omega m(1-i\omega\tau)} \quad (15)$$

In future work, the Drude model will be used to calculate the dielectric constants of the materials in the cell considering the influence of concentration of dopants.

4.5 Comparison of individual layer contributions to total reflectance

These calculations are suitable for any number of layers, as long as the thicknesses and dielectric functions of the layers are known. This cell contains thirteen finite layers, with semi-infinite air as the top layer, and a semi-infinite layer of gold on the bottom of the stack. To determine the relative contributions of each layer to the total reflectance of the cell, shown in Figure 4, the reflectance was calculated with an increasing number of layers while the change in total reflectance was recorded (weighted by intensity across all wavelengths.) For example, the reflectance of just gold against air is 0.89, and the reflectance of one 0.15 μm thick layer of MgF_2 (layer 1) between air and gold is 0.85. This decrease of 0.04 is shown as the leftmost bar in Figure 4, and this calculation was continued by adding one layer of the cell at a time. It is clear from the figure that the largest decrease in reflectance occurs when the eleventh layer is added. This is not surprising, as it is also one of the thickest layers and is one of the junctions of the cell. The GaInAs in layer eleven is 2.5 μm thick and accounts for half of the decrease in reflectance between optically thick gold and the entire cell. Adjusting the thickness of this GaInAs layer may tailor the cell to a more desirable reflectance profile.

The same method for finding the reflectance of the cell at each wavelength was repeated for 30 values of the thickness of the eleventh layer, ranging from 0.01to 4 μm. The reflectance at wavelengths below the band gap energy were weighted by the spectral radiance that also fell below the bandgap energy, to find the total reflectance below band gap energy. The same calculation was used to the find the total reflectance above the band gap energy. Figure 5 displays these values, with a varying thickness of the eleventh layer. The ideal cell would have zero reflectance above the band gap energy and reflect all radiation below the band gap energy. Results suggest that significant thinning of layer eleven can increase the below bandgap reflectance without reducing the above bandgap absorption. A limitation of this approach is that it does not consider the effect of changing the layer thickness on the internal quantum efficiency

of the cell (conversion of absorber photons to electrons in the cell.) The cell reflectance modeling framework discussed here will be used to improve the design of the cell in order to increase the below bandgap reflectance and the cell efficiency. Future implementation of the Drude model will allow more accurate properties to be used to model this cell behavior.

5. Conclusion

It is important for this thermal energy grid storage system to keep the MPV cells at a safe operational temperature by mounting the cells to an actively cooled plate. The cold plate and MPV cells will be exposed to light modeled as black body radiation at 2150°C. The thickness of

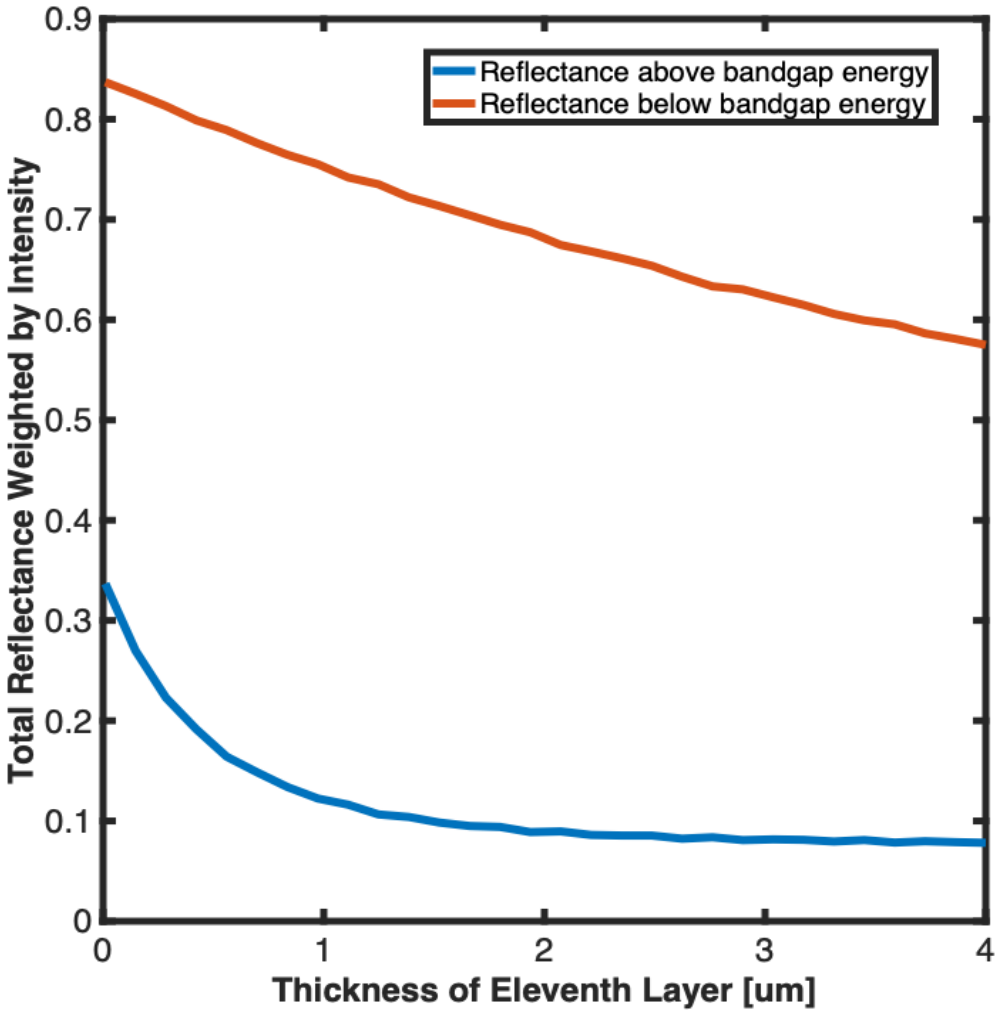

Figure 5 Reflectance above and below band gap energy vs. thickness of layer eleven.

gold plating, and the surface finish of the cold plate, is determined by reflectance measurements of gold-plated copper samples. The parasitic heat loss of the active and inactive area of the cold plate can be evaluated with a calorimeter, to aide in predicting the efficiency of an industrial sized system. The matrix transfer method for cell reflectance is used to model the absorption and reflectance of the MPV cells under this radiation. The most influential layer was determined, and total reflectance (weighted by spectral radiance) above and below the bandgap energy was calculated as a function of that layer's thickness. With experimental data the Drude model could be fitted to MPV cell materials, and in the future a more accurate model may aide in optimizing the reflectance and performance of a TPV cell and cold plate.

Appendix A: Thermal Interface Materials

Values shaded in gray are calculated from other listed values.

Product	Thermal Conductivity [W/mK]	Thickness [µm]	Thermal Resistance [m^2K/W]	Sources accessed February 2020
ARCTIC MX-4 2019 Edition	8.5	85	1E-05	https://www.amazon.com/gp/product/B07LDK4F5R/ref=ppx_yo_dt_b_asin_title_o03_s00?ie=UTF8&psc=1
Arctic Thermal Pad	6	500	8.33E-05	https://www.arctic.ac/us_en/thermal-pad.html
Deepcool Z5 High Thermal Conductivity Non-Electricity Conductive High-Density & Stable Polysynthetic Compound	1.46	6.9	1E-05	https://www.newegg.com/deepcool-z5/p/N82E16835856010
CORSAIR TM30 Performance Thermal Paste, CT-9010001-WW.	3.8	38	1E-05	https://www.newegg.com/corsair-ct-9010001-ww/p/N82E16835181166
CORSAIR XTM50 High Performance Ultra-Low Thermal Impedance CPU/GPU Thermal Compound	5	50	1E-05	https://www.newegg.com/corsair-ct-9010002-ww/p/N82E16835181180
Thermal Grizzly Kryonaut Thermal Grease Paste	12.5	125	1E-05	https://www.newegg.com/thermal-grizzly/p/13C-003E-00004
Thermal Grizzly Conductonaut Thermal Grease Paste - 1.0 Gram Model TG-C-001-R	73	730	1E-05	https://www.newegg.com/thermal-grizzly/p/2MB-001D-00002

Works Cited

[1] Joskow, Paul L. *Challenges for wholesale electricity markets with intermittent renewable generation at scale: the US experience.* Oxford Review of Economic Policy, Volume 35, Number 2, 2019, pp 291-331.

[2] Kumar, N.; Besuner, P. et al. *Power Plane Cycling Costs.* National Renewable Energy Laboratory, April 2012, DOI: 10.2172/1046269.

[3] Amy, Caleb; Seyf, Hamid Reza; Steiner, Myles A.; Friedman, Daniel J.; and Henry, Asegun; *Thermal energy grid storage using multi-junction photovoltaics* Energy Environ. Sci*.,* 2019, 12, 334, DOI: 10.1039/c8ee02341g.

[4] See Appendix A

[5] FluxTeq HTHFS-01 Product Specifications, accessed May 8, 2020. www.fluxteq.com/hthfs-high-temperature-heat-flux-sensor-1

[6] International Thermal Instrument Company, Inc Product Specifications, accessed May 8, 2020. thermalinstrumentcompany.com/products/heatfluxtransducers/standardthermalfluxmeters

[7] Chen, Gang. *Nanoscale Energy Transport and Conversion.* Oxford University Press, March 3, 2005, pp 159-218.

[8] Olmon, Robert L. Et al. *Optical dielectric function of gold.* Physical Review B 86, 235147, December 2012. DOI: 10.1103/PhysRevB.86.235147.

[9] Carlson, Dean. "RE: Quote" Received by Lucy Milde, February 18, 2020.

[10] Seyf, Hamid Reza; Henry, Asegun; *Thermophotovoltaics: a potential pathway to high efficiency concentrated solar power* Energy Environ. Sci*.,* 2016, 9, 2654, DOI: 10.1039/c6ee01372d, p 2660.

[11] H. H. Li. Refractive index of alkaline earth halides and its wavelength and temperature derivatives. *J. Phys. Chem. Ref. Data* **9**, 161-289 (1980) and references therein. https://doi.org/10.1063/1.555616 *Accessed on* refractiveindex.info, *2020.*

[12] M. Schubert, V. Gottschalch, C. M. Herzinger, H. Yao, P. G. Snyder and J. A. Woollam. Optical constants of $Ga_xIn_{1-x}P$ lattice matched to GaAs, *J. Appl. Phys.* **77**, 3416 (1995). https://doi.org/10.1063/1.358632 *Accessed on* refractiveindex.info, *2020.*

[13] S. Adachi. Optical dispersion relations for GaP, GaAs, GaSb, InP, InAs, InSb, $Al_xGa_{1-x}As$, and $In_{1-x}Ga_xAs_yP_{1-y}$, *J. Appl. Phys.* **66**, 6030-6040 (1989). https://doi.org/10.1063/1.343580 *Accessed on* refractiveindex.info, *2020.*

[14] R. L. Olmon, B. Slovick, T. W. Johnson, D. Shelton, S.-H. Oh, G. D. Boreman, and M. B. Raschke. Optical dielectric function of gold, *Phys. Rev. B* **86**, 235147 (2012) (see Supplemental Material for numerical data) https://doi.org/10.1103/PhysRevB.86.235147 *Accessed on* refractiveindex.info, *2020.*

[15] Tsurimaki, Yoichiro. *Transfer matrix method.* Course materials for 2.58 Radiative Transfer, MIT, Spring 2020.

[16] Dresselhaus, M. S. *Solid State Physics Part II: Optical Properties of Solids.* Course materials for 6.732 Solid State Physics, MIT, Fall 2001. Accessed May 8, 2020. http://web.mit.edu/6.732/www/texts.html